Journal of Rare Earths 39 (2021) 297–304

Contents lists available at ScienceDirect

Journal of Rare Earths

journal homepage: http://www.journals.elsevier.com/journal-of-rare-earths

$LaO_x(OH)_y$ supported platinum catalysts for CO oxidation: Deactivation by formation of lanthanum carbonate☆

Luozhen Jiang [a, d], Junxiang Chen [c], Rui Si [a, b, *]

[a] Shanghai Institute of Applied Physics, Chinese Academy of Sciences, Shanghai 201204, China
[b] Shanghai Synchrotron Radiation Facility, Zhangjiang Laboratory, Shanghai 201204, China
[c] Division of China, TILON Group Technology Limited, Shanghai 200090, China
[d] University of Chinese Academy of Sciences, Beijing 100049, China

ARTICLE INFO

Article history:
Received 7 November 2019
Received in revised form
15 February 2020
Accepted 24 February 2020
Available online 28 February 2020

Keywords:
Platinum catalyst
Lanthanum oxide
Lanthanum hydroxide
CO oxidation
Structure–activity relationship
Rare earths

ABSTRACT

Platinum catalyst for CO oxidation has been studied for decades, due to its high activity and good stability. In this work, we prepared three different lanthanum oxide or hydroxide supports ($LaO_x(OH)_y$), and deposited platinum (Pt) with 0.5 at% via an impregnation approach to synthesize $Pt/LaO_x(OH)_y$ catalysts. However, we find that these catalysts perform a poor stability for the CO oxidation reaction. The fresh and used samples were comprehensively characterized by multiple techniques including power X-ray diffraction (XRD), X-ray absorption fine structure (XAFS), transmission electron microscopy (TEM), temperature-programmed reduction by carbon monoxide (CO-TPR) and thermogravimetric analysis (TGA), to demonstrate that the oxidized platinum atoms or clusters, without any component of Pt–Pt metallic bond, are highly dispersed on the surface of $LaO_x(OH)_y$. Furthermore, the as-formed lanthanum carbonate ($La_2O_2CO_3$) during the exposure to ambient circumstances or in the reaction atmosphere of CO + O_2, severely impair the reactivity of $Pt/LaO_x(OH)_y$. On the basis of the obtained experimental results, we have drawn a conclusion that the oxidized PtO_x atoms or Pt_xO_y clusters are the active species for CO oxidation, while the formation of lanthanum carbonate is the origin of deactivation on reactivity.

1. Introduction

The oxidation of CO, although one of the simplest catalytic reactions known, is very important for both practical use and fundamental research. At present, supported metal catalyst for CO oxidation reaction has been studied for decades,[1–11] and lots of research groups reported that the supported platinum (Pt) catalysts are very active for this reaction.[12,13] Among them, reducible oxides such as CeO_2, FeO_x, TiO_2[14–16] seemed to be good candidates for the support. For instance, Pt single-atoms on FeO_x showed extremely high performance for CO oxidation because of the unique properties of atomically dispersed Pt species.[17] Another example is that Pt–O–Ce with a low coordination number with oxygen under realistic conditions, could contribute to the efficient activity when Pt was supported by CeO_2.[18] For another report, the Pt^{2+}/Pt^0 coupled with Ce^{4+}/Ce^{3+} in Pt/CeO_2 catalyst via oxygen vacancy is suggested to facilitate low-temperature redox reactions.[19] Indeed, Moses-DeBusk et al. found that a supported Pt single-atom prefers to be bound to O_2 over CO first, and then CO reacts with the oxygenated Pt atom to form carbonate to further release CO_2.[20]

Rare earth oxide can be widely applied in catalysis, i.e. cerium oxide (CeO_2) was used as an active support for the water-gas shift (WGS) reaction.[21] In 2003, Wang and Li reported the synthesis of lanthanum hydroxide ($La(OH)_3$) with different morphologies via a hydrothermal method.[22] However, till now, very few results on lanthana-supported metal catalysts have been investigated.[23–26] For instance, Li et al. *in situ* deposited 14 nm Ag nanoparticles on the surface of $La(OH)_3$ nanorods to form framework composites to be further tested for CO oxidation.[27] On the other hand, by air-calcination, $La(OH)_3$ can be converted to basic oxide LaOOH at 360 °C ($La(OH)_3 \rightarrow LaOOH + H_2O$) and then La_2O_3 at 650 °C ($LaOOH \rightarrow La_2O_3 + H_2O$).[28] These phase transformations may enrich the structural features of lanthana to support metal catalysts such as $Pt\text{-}LaO_x(OH)_y$. Furthermore, lanthanum oxide could also be

☆ **Foundation item:** Project supported by the National Natural Science Foundation of China (21773288) and National Key Basic Research Program of China (2017YFA0403402).
* Corresponding author.
E-mail address: sirui@sinap.ac.cn (R. Si).

https://doi.org/10.1016/j.jre.2020.02.016
1002-0721/

transferred to carbonate ($La_2O_2CO_3$) when exposed to CO_2 or ambient air.[29] It has been reported that the modified metal (Pt)-support ($LaO_x(OH)_y$) interaction could be the driving force for CO_2 reforming of methane,[30] but the effect of as-formed lanthanum carbonate was rarely studied for redox reaction including CO oxidation.

To obtain the reliable structure-activity relationship, advanced characterization techniques are required to precisely detect the complex structural properties of supported metal or metal oxide nanocatalysts. As for heterogeneous catalysis, X-ray absorption fine structure (XAFS) technique have been broadly applied to the analyses of the structural evolution of low-concentration active metal or metal oxide species. Particularly, X-ray near edge spectroscopy (XANES) and extended X-ray absorption fine structure (EXAFS) parts are effective for the determination of both electronic structure (oxidation state, charge transfer, etc.) and local coordination structure (coordination number, bond distance, etc.) up to 0.6–0.8 nm, respectively.[31,32] For example, Yin et al. identified five-coordinated C_1–Pt–Cl_4 species and a four-coordinated C_2–Pt–Cl_2 species in Pt-GDY1 and Pt-GDY2, respectively.[33]

In this work, we prepared three different types of lanthana supports, i.e., hydroxide $La(OH)_3$ via a hydrothermal approach at 200 °C, and oxyhydroxide LaOOH or oxide La_2O_3 after the sequential air-calcination at 400 or 800 °C, respectively. Platinum species are deposited onto the matrix via an impregnation route to produce Pt-$LaO_x(OH)_y$ catalysts. These as-dried or as-calcined samples were measured in CO + O_2 atmosphere for the catalytic oxidation of CO reaction, and all of the investigated catalysts show severe decay on activity vs time-on-stream during the stability tests. On the basis of multiple characterization results on power X-ray diffraction (XRD), XAFS, transmission electron microscopy (TEM), temperature-programmed reduction by carbon monoxide (CO-TPR) and thermogravimetric analysis (TGA), we have drawn a conclusion that the oxidized PtO_x atoms or Pt_xO_y clusters are the active species for CO oxidation, while the formation of lanthanum carbonate is the origin of deactivation.

2. Experimental

2.1. Catalyst preparation

All the chemicals used in this work were of analytical grade and purchased from Sinopharm Chemical Reagent Co., Ltd. without any further purification, and the gases were all purchased from Shanghai Weichuang Co., Shanghai, China.

The $La(OH)_3$ nanosheets were synthesized according to the hydrothermal method. $La(NO_3)_3{\cdot}6H_2O$ (41.6 mmol) was add to an aqueous solution with 35 mL H_2O and 160 mL alcohol, then, an aqueous KOH (4 mol/L) was added into solution to adjust the PH to be 12 and following with vigorous stirring about 30 min. After the precipitation process was completed, the stock solution was transferred into a Teflon bottle (inner volume: 100 mL), and further tightly sealed in a stainless-steel autoclave. The hydrothermal procedure was carried out in a temperature-controlled electric oven at 200 °C for 24 h. Then, the precipitates were washed by Millipore (>18 MΩ) water four times and ethanol once. The $La(OH)_3$ nanosheets were obtained by drying the as-washed product in vacuum at 80 °C for 12 h and further calcined in air at 200 °C for 4 h (heating rate: 2 °C/min).

The LaOOH nanosheets were prepared by $La(OH)_3$ with calcining in air at 400 °C for 4 h (heating rate: 2 °C/min), and the La_2O_3 nanosheets were calcined in air at 800 °C for 4 h (heating rate: 2 °C/min).

$LaO_x(OH)_y$ supported platinum catalyst was synthesized via an initial wet-impregnation method. 5 mg of tetra-ammine-platinum (II) nitrate was dissolved in to 100 μL H_2O and then 0.5 g sample of $LaO_x(OH)_y$ support was added by stirring with a medicine spoon, continuing dropwise adding H_2O until support reaching saturated water absorption with following stirring for 15 min. The precipitation was then dried in air at room temperature and following dried in vacuum at 80 °C for 12 h and further calcined in air at 300 °C for 4 h (heating rate: 2 °C/min) to obtain 0.5 wt% Pt/$LaO_x(OH)_y$.

2.2. Characterizations

The metal atom ratios of Pt/La were determined by inductively coupled plasma atomic emission spectroscopy (ICP-AES) on an IRIS Intrepid II XSP instrument (Thermo Electron Corporation).

The nitrogen adsorption-desorption characterizations were tested on an ASAP2020-HD88 analyzer (Micromeritics Co., Ltd.) at 77 K. The tested powders were degassed at 250 °C under vacuum (<100 mm Hg) for 4 h before the injection of N_2. The BET specific surface areas (S_{BET}) were obtained from data in the relative pressure ranging between 0.05 and 0.20.

The powder X-ray diffraction (XRD) patterns were tested on a Bruker D8 Advance diffractometer (40 kV and 40 mA) or a Malvern Panalytical X Pert powder diffractometer (40 kV and 40 mA), with Cu Kα1 radiation ($\lambda = 0.15406$ nm) at a scanning rate of 4 (°)/min. The 2θ angles were calibrated by a μm-scale alumina (α-Al_2O_3) standard. The diffraction patterns were scanned from 10° to 90° with a step of 0.02°. The ground sample was placed into a quartz sample holder before each test.

The transmission electron microscopy (TEM), high-resolution transmission electron microscopy (HRTEM) images and scanning transmission electron microscopy-energy dispersive spectroscopy (STEM-EDS) elemental mapping results were obtained from an FEI Tecnai G2 F20 microscope executed at 200 kV, equipped with a Genesis XM2 accessory (EDAX Inc.). All the tested samples were sonicated in ethanol for about 5 min, and then a drop of liquid supernatant was placed on an ultra-thin (3–5 nm) carbon film-coated Mo grid. After dried spontaneously under dark conditions, the sample grid was inserted into the sample holder.

The X-ray absorption fine structure (XAFS) spectroscopy at the Pt L_3 ($E_0 = 11{,}564$ eV) edge was operated at 3.5 GeV in "top-up" mode with a constant current of 240 mA at the BL14W1 beamline of the Shanghai Synchrotron Radiation Facility (SSRF). The XAFS data were recorded under Fluorescence mode with a 7-element Ge solid state detector for Pt. The absorption of Pt foil was used to calibrate the X-ray energy. The data of XAFS were extracted by Athena and the profiles were fitted by Artemis codes.

For the X-ray absorption near edge structure (XANES) part, the experimental absorption coefficients as a function of energies $\mu(E)$ were reported as "normalized absorption" processed by background subtraction and normalization procedures. Using the Athena software, the chemical valence of Pt was calculated by linear combination fitted with the comparison to the corresponding references of Pt/PtO_2 based on the normalized XANES profiles.

For the extended X-ray absorption fine structure (EXAFS) part, the Fourier transformed (FT) data in R space was calculated by applying quick first shell model for Pt–O contributions. The passive electron factors S_0^2 were obtained by fitting the experimental data on Pt foils by fixing the coordination number (CN) of Pt–Pt to be 12, and then fixed for further analysis of the measured sample. The parameters were allowed to vary during the fit process which was used to describe the electronic properties (e.g., correction to the photoelectron energy origin E_0) and local structure environment including CN, bond distance (R) around the absorbing atoms, and the Debye-Waller (σ^2) factor was set to be 0.00003 nm^2. The fitted ranges for k and R spaces were all selected to be $k = 20$–100 nm^{-1} with $R = 0.1$–0.22 nm (k^3 weighted).

2.3. Catalytic tests

The temperature-programmed reduction by carbon monoxide (CO-TPR) was conducted in a chemisorption apparatus (AutoChem II, Micromeritics Co., Ltd.) equipped with a thermal conductivity detector (TCD). The 50 mg laminar and sieved samples (40–60 mesh) were pretreated under O_2 (5% O_2/He) flow at 300 °C for 30 min and cooled naturally to room temperature before reduction. The reduction process was performed with a gas mixture of 5% CO/He (Shanghai Weichuang Co., 99.997% purity) from room temperature to 500 °C (flowing rate: 20 mL/min; heating rate: 5 °C/min). The variations of H_2 and CO_2 in outlets were monitored by a mass spectrometer (LC-D200M, TILON Co., Ltd.).

The CO oxidation activities for $LaO_x(OH)_y$-supported platinum samples was estimated in a AutoChem II. The 30 mg of sieved (40–60 mesh) samples were pretreated in O_2 (5% O_2/He) at 200 °C for 30 min before test and cooled down to room temperature in pure He. Then, the pretreated samples were passed a gas mixture of 1% O_2/2% CO/He (99.997% purity, Shanghai Weichuang Co.) at a flow rate of 30 mL/min, corresponding to a space velocity of 60000 mL/(h·g_{cat}). A gas chromatograph (Micro GC Fusion, Inficon Co., Ltd.) was used to monitor the variations of CO and CO_2 in outlets. The CO conversion was calculated with the equations of "CO conversion (%) = CO_{2out}/(CO_{2out} + CO_{out}) × 100". In the stability experiments, the reaction temperature was 250 °C.

The test of catalytic WGS reaction activities was tested in the plug flow reactor, and the thermocouple was placed on the top of the catalysts and connected with a PID controller. Before test, a 5% H_2/Ar gas mixture was fed to 63 mg of sieved (40–60 mesh) sample at 300 °C for 30 min and cooled to room temperature in pure N_2. Then the catalytic activity of WGS reaction was test under reactant gas consisting of 2 vol% CO/N_2 (99.997% purity, Jinan Deyang Co.) mixed with water vapor (CO:H_2O = 1:5) at a flow rate of 63 mL/min to obtain a GHSV of 60000 mL/(h·g_{cat}). The reactant temperature began from 150 to 400 °C under the heating rate 5 °C/min and hold for 1 h at 150, 200, 250, 300, 350, and 400 °C, respectively. Then, the catalytic data were recorded at 150, 200, 250, 300, 350 and 400 °C. The CO conversion of WGS was calculated according to the following equation: CO conversion (%) = (CO_{in} − CO_{out})/CO_{in} × 100. And variations of CO and CO_2 in outlet gases were monitored by a Gasboard 3500 IR spectroscope (Wuhan Sifang Co.).

The thermogravimetric analysis (TGA) in O_2 or CO_2 and were estimated in a TGA/DSC 3+ (METTLER TOLEDO Co., Ltd., Swiss Confederation). The variations of H_2O and CO_2 in outlets were monitored by a LC-D200M mass spectroscope. The 10 mg of samples was added to an aluminum oxide crucible in O_2 (5% O_2/He, 5 mL/min) or CO_2 (5% CO_2/He, 5 mL/min), heating up from 30 to 1000 °C at a heating rate of 5 °C/min. The off-gas was injected to a mass spectroscope which detected the m/z signal of 18 (H_2O) and 44 (CO_2).

3. Results and discussion

The $La(OH)_3$ support was prepared via a hydrothermal approach, and then was measured by TGA to probe its thermal stability. Fig. 1(a) shows that the LaOOH phase formed at 200–300 °C, and the La_2O_3 component started to be produced after 400 °C. So, we calcined the $La(OH)_3$ support at 400 and 800 °C to obtain the LaOOH and La_2O_3 supports, respectively. The crystal structure of each $LaO_x(OH)_y$ support was characterized by XRD. Fig. 1(b) shows that $La(OH)_3$ and La_2O_3 are of pure phases, while LaOOH is a mixture of $La(OH)_3$, LaOOH and $La_2O_2CO_3$. The presence of $La_2O_2CO_3$ indicates that $La(OH)_3$ absorbed CO_2 to form carbonates in ambient air after the calcination step at 400 °C, since the previous report shows that the $La(OH)_3$ could be completely transformed to $La_2O_2CO_3$ if calcined at 500 °C for 3 h in air.[34]

The TEM and HRTEM images were used to verify the morphology of $LaO_x(OH)_y$ supports. Specifically, $La(OH)_3$ (Fig. 2(a)) and LaOOH (Fig. 2(b)) supports are of irregular nanosheet; while La_2O_3 is composed by big particles (Fig. 2(c)). Previously, $La(OH)_3$ and $La_2O_2CO_3$ nanorods have been reported with the surface areas of 84.95[22] and 52.7 m^2/g,[35] respectively. Here, we uniquely prepared the $La(OH)_3$ and LaOOH nanosheets and further used them as supports for platinum deposition. The HRTEM images in Fig. 2(d–f) display the clear interplanar spacing to identify the presence of $La(OH)_3$, LaOOH and La_2O_3, respectively, which is consistent with the XRD results. The BET surface areas (S_{BET}) values of supports (see Table 1) are lower than the morphology of nanorods reported before, demonstrating the smaller exposed surface in this work. Table 1 also shows that the S_{BET} of La_2O_3 is obviously lower than that of the other two supports, corresponding to its larger particle size in TEM.

The ICP-AES analysis results in Table 1 show that the atom ratios of Pt in Pt/$La(OH)_3$, Pt/LaOOH and Pt/La_2O_3 are 0.58%, 0.57% and 0.48%, respectively, closed to the designed value (0.5%). The "light-off" profiles of CO oxidation reaction (2CO + O_2 = 2CO_2) with a space velocity of 60000 mL/(h·g_{cat}) or WGS reaction (CO + H_2O = CO_2 + H_2) with a space velocity of 60000 mL/(h·g_{cat}) were used to evaluate the catalytic performance of $LaO_x(OH)_y$-supported platinum samples. Fig. 3 show that Pt/LaOOH performed higher values of 50% CO conversions than those of Pt/$La(OH)_3$ and Pt/La_2O_3 (see Table 1). Pt/$La(OH)_3$ behaved the lowest reactivity for both CO

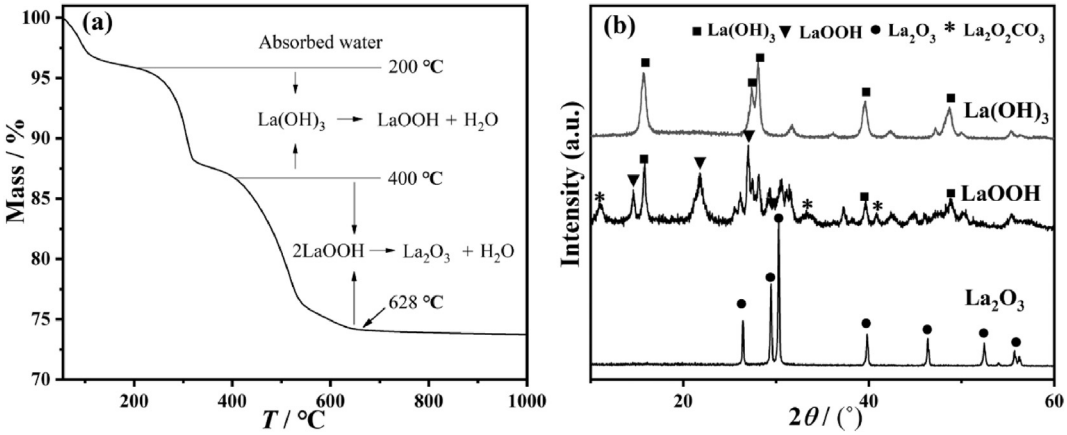

Fig. 1. TGA curve of $La(OH)_3$ under O_2 flow (a) and XRD patterns of $LaO_x(OH)_y$ supports (b).

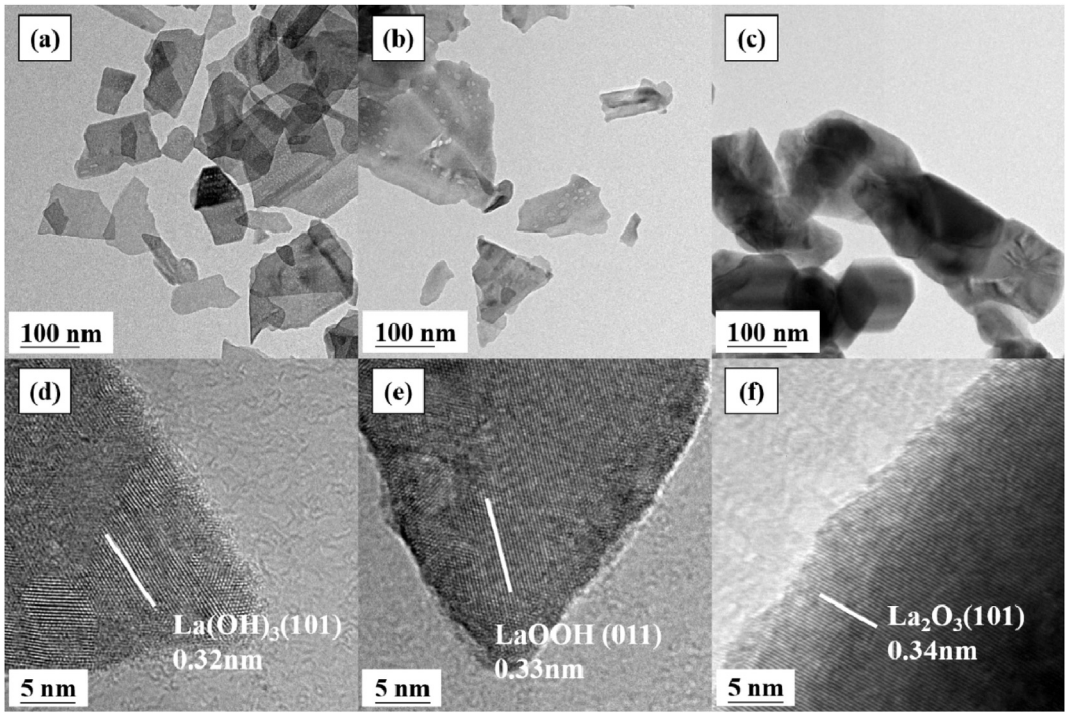

Fig. 2. TEM images (a–c) and HRTEM (d–f) images of $LaO_x(OH)_y$. (a, d) $La(OH)_3$; (b, e) LaOOH; (c, f) La_2O_3.

oxidation and WGS reactions, even with the highest BET surface area (34 m^2/g). For the key steps of the WGS reaction catalysis (CO adsorption and H_2O activation) occurs on oxidized Pt sites[36] and the metallic Pt^0 species are active for the low-temperature CO oxidation reaction,[37] the reported catalyst normally performed inverse activity between CO oxidation and WGS reactions. However, in this work, the supported platinum samples exhibited similar trend for both of the measured reaction. Thus, for the further investigations of structure-activity relationship on $La(OH)_xO_y$-supported platinum catalysts, we only focus the discussion on the CO oxidation reaction.

To probe the active species, we carried out multiple characterization techniques to detect the structural evolution before and after the reaction. The XRD patterns (Fig. 4) of fresh and used samples and the HRTEM/STEM-HADDF images (Fig. 5) of the used samples for CO oxidation also show that calcined processes of catalyst preparation generated the carbonate and the reaction processes formed carbonate. Obviously, $La_2O_2CO_3$ phase was identified for both fresh and used catalysts. Meanwhile, LaOOH vanished after the CO oxidation reaction for Pt/LaOOH (Fig. 4(b)), revealing that all the LaOOH species were transformed into carbonates. Clearly, no crystallized Pt components are presented over the supports of $LaO_x(OH)_y$ from the HRTEM images in Fig. 5(a–c) and the related STEM-HADDF results (Fig. 6(d–i)). So, platinum species were well dispersed on the studied support, probably in the form of single atoms or ultra-fine clusters. Therefore, on the basis of above XRD and TEM data, the alter of support structure to carbonates could not modify the Pt dispersion, but indeed change the catalytic activity.

Table 1
BET specific surface areas (S_{BET}) of $LaO_x(OH)_y$ support, atomic ratios of Pt (C_{Pt}) and the 50% conversion (T_{50}) for CO oxidation or water-gas shift reaction of platinum catalysts supported on $LaO_x(OH)_y$.

Sample	S_{BET}[a] (m^2/g)	C_{Pt}[b] (at%)	T_{50} (CO oxidation)[c] (°C)	T_{50} (Water-gas shift)[c] (°C)
$Pt/La(OH)_3$	34	0.58	250	355
Pt/LaOOH	27	0.57	218	290
Pt/La_2O_3	5	0.48	247	320

[a] Calculated from nitrogen adsorption results.
[b] Determined by ICP-AES.
[c] Calculated from the light-off profiles.

The XAFS experiments were used to identify the platinum species for both electronic structure (oxidation state of Pt) and short-range coordination structure (Pt–O or Pt–Pt shell). Fig. 6(a) and Table 2 show the XANES profiles and the calculated averaged oxidation state of Pt, which were done via the liner combination fits,[38] with the help of various standards of Pt foil (Pt^0) and PtO_2 (Pt^{4+}). Obviously, the $Pt/La(OH)_3$ performs the highest Pt valence (+3.43), while the Pt/La_2O_3 behind it (+3.26). Notably, the Pt/LaOOH performs the lowest valence (+2.84) while it obtained the highest activity. Combining the "light-off" curves (Fig. 4(a)), it can be verified that the lower oxidation state leads to the higher activity on CO oxidation. Fig. 7(b) and Table 1 show the EXAFS fitting results on the used catalysts. The strong peak at *ca.* 0.20 nm (CN ≈ 4) is identified for the first shell of all the tested samples for Pt L_3-edge, which is contributed by the PtO_x single-ions or Pt_xO_y ultra-fine clusters. The origin oxygen may be the strongly chemisorbed oxygen.[39] The absence of further shells for either Pt–Pt (Pt–O–Pt) and Pt–La (Pt–O–La) indicates that the PtO_x or Pt_xO_y species may be highly dispersed on the surface of $LaO_x(OH)_y$. Combining with "light-off" profiles (Fig. 3(a)) and CO-TPR data (Fig. 7(d)), we drew a conclusion on the intrinsic activity of PtO_x or Pt_xO_y, and the lower valence of Pt was beneficial to the higher activity.

The TG-MS was used to identify the creation of carbonate of La during synthesis and the catalytic reaction (Fig. 7). Fig. 7(a) shows that the mass loss ratio before 100 °C was the absorbed water at TG curve; and at 280–300 °C, the hydroxyl loss in the form of water occurred; after 560 °C, the carbonate was decomposed to form CO_2 confirmed by MS spectrometry.[40] Thus, we can figure out the mass

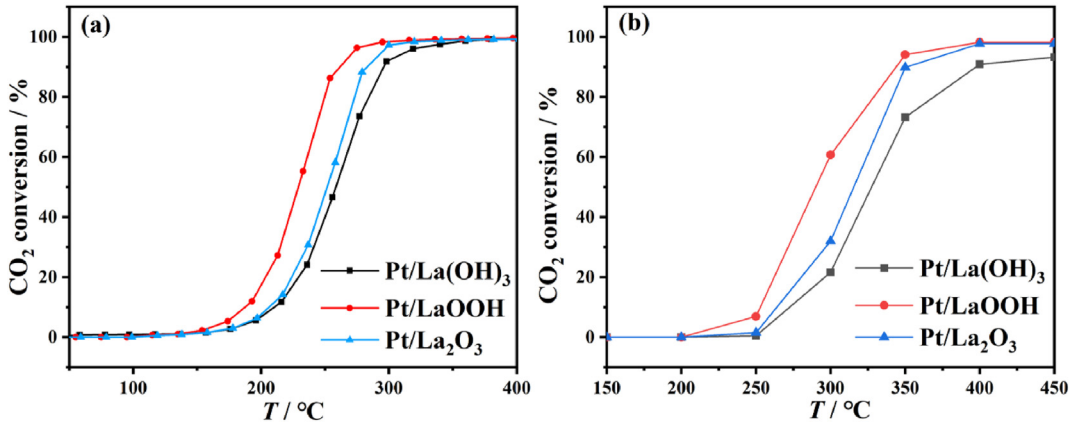

Fig. 3. "Light off" for CO oxidation (a) and WGS reaction (b).

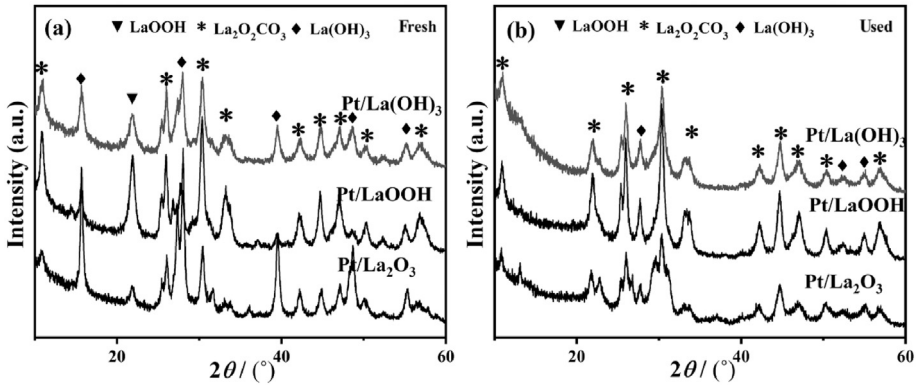

Fig. 4. XRD patterns of Pt/LaO$_x$(OH)$_y$ catalysts: fresh (a) and used (b) after CO oxidation.

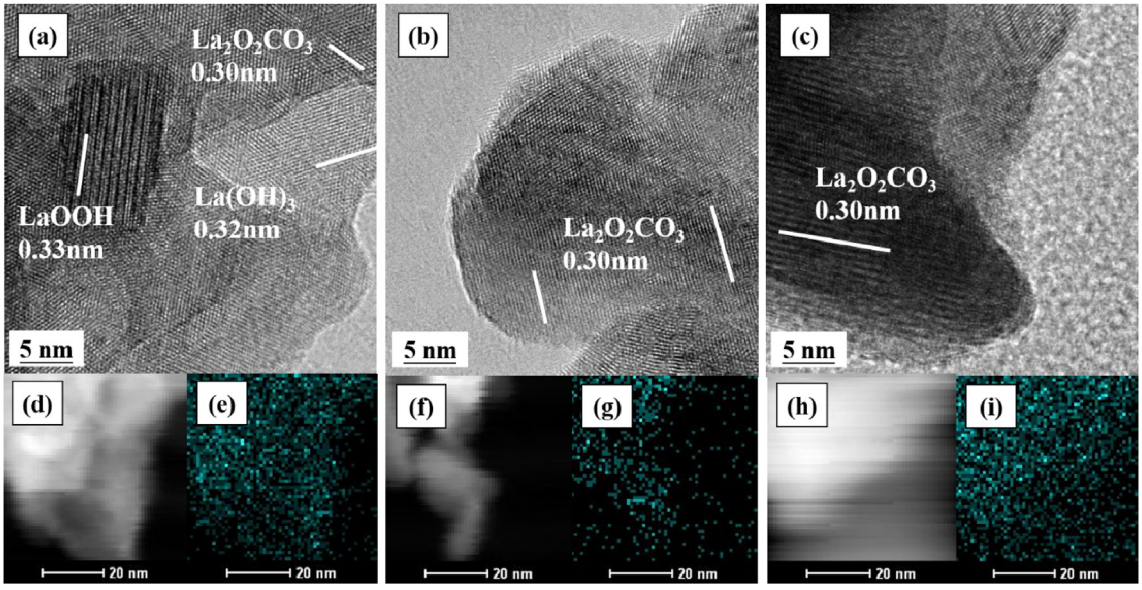

Fig. 5. HRTEM images (a–c) and STEM-HADDF/EDS elemental mapping results (d–i) of used Pt/LaO$_x$(OH)$_y$ catalysts. (a, d, e) Pt/La(OH)$_3$; (b, f, g) Pt/LaOOH; (c, h, i) Pt/La$_2$O$_3$.

rate of 7.38% of carbonates in the catalyst preparation. In addition, the TG-MS curves of used sample are shown in Fig. 7(b). Here, almost no water signal was defined, indicating that after reaction all the LaOOH support was consumed completely by the generated CO_2 during reaction. Indeed, the mass loss rate of TG (9.61%) after 560 °C was in good accord with the MS peak of CO_2, which was higher than that for the fresh sample (7.38%), demonstrating that the creation of extra carbonates during the CO oxidation reaction.

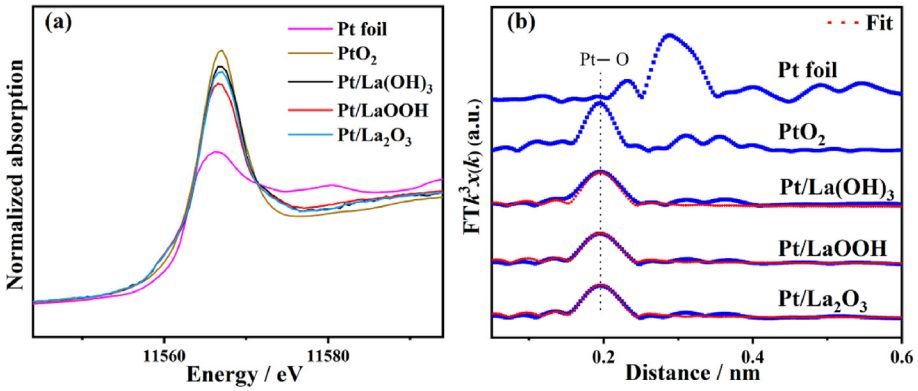

Fig. 6. XANES profiles (a) and EXAFS spectra (b) with fits in R space of Pt L_3 edge for $LaO_x(OH)_y$-supported catalysts which were used in CO oxidation reaction.

Table 2
Averaged oxidation state of iron (δ) and Pt L_3-edge EXAFS fitting results (R: distance; CN: coordination number; σ^2: Debye-Waller factor; ΔE_0: inner potential correction) of $Pt/LaO_x(OH)_y$ samples.

Sample	δ[a]	Pt—O		σ^2 ($\times 10^{-2}$ nm^2)	ΔE_0 (eV)
		R ($\times 10^{-1}$)	CN		
$Pt/La(OH)_3$	+3.43	2.01 ± 0.02	4.1 ± 0.5	0.003	10.3 ± 2.4
Pt/LaOOH	+2.84	1.99 ± 0.02	4.0 ± 0.4		8.9 ± 2.2
					9.3 ± 2.0
Pt/La_2O_3	+3.26	2.01 ± 0.02	3.6 ± 0.3		

[a] Determined by linear combination analysis on the XANES profiles with references of Pt foil ($\delta = 0$)/PtO_2 ($\delta = 4$).

To find out the formation during the calcination step, we further tested $La(OH)_3$ under the CO_2 flow (Fig. 7(c)). It can be obviously demonstrated that the formation of carbonate and the hydroxyl decomposing occur at the same temperature period between 200 and 400 °C. However, after 750 °C, the generated carbonates began to be decomposed into La_2O_3. This demonstrates that the supports could form carbonates during the air-calcination or catalytic process for CO oxidation and WGS reactions.

To investigate the relatively well activity for CO Oxidation of Pt/LaOOH sample for CO oxidation and WGS reaction, we also proceeded a temperature-programmed reduction by carbon monoxide

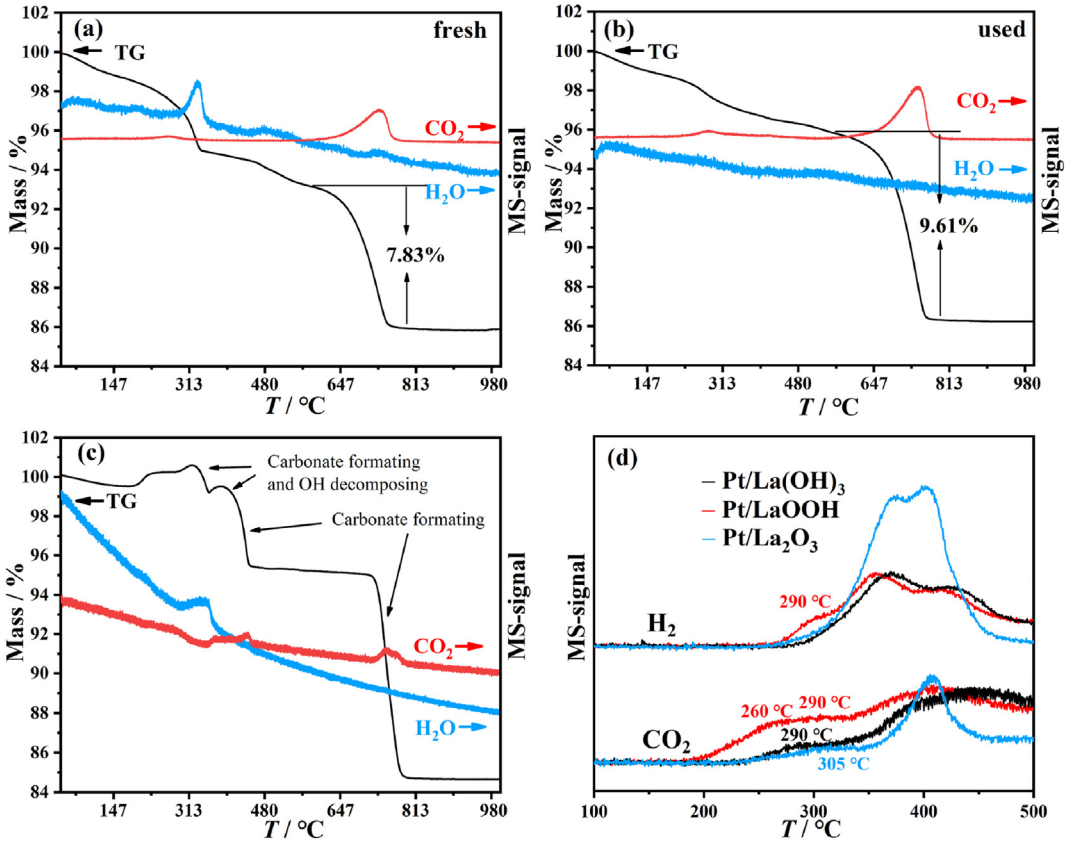

Fig. 7. TG-MS analysis of fresh (a) and used (b) Pt/LaOOH sample at a flow rate of 5 mL/min in 5% O_2/He in a heating rate of 5 °C/min; (c) $La(OH)_3$ support at a flow rate of 5 mL/min in 5% CO_2/He at a heating rate of 5 °C/min; (d) Carbon monoxide temperature programmed reduction (CO-TPR) patterns of $Pt/LaO_x(OH)_y$ catalysts tested at the same conditions and the same unit and at a heating rate of 5 °C/min and flow rate of 30 mL/min in 5% CO/He.

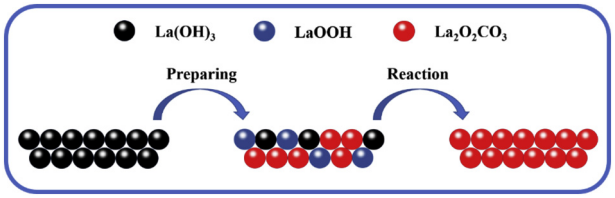

Fig. 8. Structural demonstration of support LaOOH transformation for process of preparing and CO oxidation.

(CO-TPR) experiment of these three catalysts (Fig. 7(d)). For all the samples, the present of reduction peak of surface oxide (Fig. 7(d), 260 °C for Pt/LaOOH, 290 °C for Pt/La(OH)$_3$ and 305 °C for Pt/La_2O_3) manifests that the addition of Pt enhanced the quantity of surface oxide and increased reducibility of $LaO_x(OH)_y$ and may form a PtO_x or Pt_xO_y species in comparison to their supports themselves,[36] combined with the XAFS result (Fig. 6 and Table 2). For the Pt/LaOOH, the reduction peak of surface oxide (Fig. 7(d)) appears at a lower temperature 260 °C and we obtained a taller peak which was belong to the reduction of PtO_x or Pt_xO_y, indicating that the surface oxide of LaOOH prefers to form a PtO_x or Pt_xO_y species with Pt and the quantity was more than other two supports, indicating that the removing of surface hydroxyl groups via a calcining process at 400 °C could expose more surface oxygen. This may be the reason of a better activity than others. It is diverting that the "light-off" temperature of CO oxidation (Fig. 3(a)) is consistent with the CO-TPR curve (Fig. 7(d)), which shows that the temperature of PtO_x or Pt_xO_y reduction was the temperature of CO oxidation, demonstrating that PtO_x or Pt_xO_y should be the active species. The inactivity of $LaO_x(OH)_y$ support could explain this view more adequately. The following peaks after 320 °C of CO-TPR curves (Fig. 7(d)) including H_2 and CO_2 peaks are generated from surface hydroxyl group and bulk hydroxyl group, respectively.[41] They may not contribute to the CO oxidation reaction, but they are more active to WGS reaction,[21,36] and the WGS reaction test could explain distinctly (Fig. 3(b)).

By the aids of multiple characterization techniques, we now have a full view on the"support-effect" relationship of LaOOH-supported platinum catalyst (Fig. 8). From the "light-off" curves (Fig. 3(a)), we guess that the LaOOH calcined at 400 °C from La(OH)$_3$ may generate more surface oxide to interact with Pt to form PtO_x or Pt_xO_y which are the activity species of the reaction. The XANES profiles identify the fully oxidized Pt oxidation state (Table 2), and the EXAFS results verify the presence of the highly dispersed PtO_x or Pt_xO_y, however, for the $LaO_x(OH)_y$-supported platinum catalyst, preventing the generating of carbonate and controlling synthesis of LaOOH to form more PtO_x or Pt_xO_y species are still interesting issues.

4. Conclusions

In summary, we synthesized a $LaO_x(OH)_y$-supported platinum catalyst via an impregnation approach. We confirmed that the Pt/LaOOH performs a better activity for CO oxidation and WGS reaction than the Pt/La(OH)$_3$ and Pt/La_2O_3 counterparts due to the surface areas and the exposed surface oxides. With the assistance of multiple characterization approaches including CO-TPR and XAFS, we identified that the PtO_x or Pt_xO_y species is the only active site for CO oxidation and WGS reactions, while the lower oxidation state leads to the higher activity. In addition, we demonstrate that the generated carbonate species from the process of synthesis and/or reaction leads to a low activity and rapid deactivation, with the help of TGA. Hence, we demonstrate that the critical issue to improve the activity of hydroxide-supported catalysts ($LaO_x(OH)_y$) is to prevent the formation of carbonates and to disperse more surface hydroxyl groups, which can interact with the active metal.

References

1. Wang WW, Yu WZ, Du PP, Xu H, Jin Z, Si R, et al. Crystal plane effect of ceria on supported copper oxide cluster catalyst for CO oxidation: importance of metal–support interaction. *ACS Catal*. 2017;7(2):1313.
2. Du PP, Wang WW, Jia CJ, Song QS, Huang YY, Si R. Effect of strongly bound copper species in copper-ceria catalyst for preferential oxidation of carbon monoxide. *Appl Catal, A*. 2016;518:87.
3. Bollinger MA, Vannice MA. A kinetic and DRIFTS study of low-temperature carbon monoxide oxidation over Au-TiO_2 catalysts. *Appl Catal B*. 1996;8(4):417.
4. Shu M, Wei S, Jia CJ, Wang DL, Si R. Effect of nickel oxide doping to ceria-supported gold catalyst for CO oxidation and water-gas shift reactions. *Catalysts*. 2018;8(12):584.
5. Du PP, Hu XC, Wang X, Ma C, Du M, Zeng J, et al. Synthesis and metal-support interaction of subnanometer copper–palladium bimetallic oxide clusters for catalytic oxidation of carbon monoxide. *Inorg Chem Front*. 2017;4(4):668.
6. Wu Z, Li M, Overbury SH. On the structure dependence of CO oxidation over CeO_2 nanocrystals with well-defined surface planes. *J Catal*. 2012;285(1):61.
7. Wang XL, Fu XP, Wang WW, Ma C, Si R, Jia CJ. Effect of structural evolution of gold species supported on ceria in catalyzing CO oxidation. *J Phys Chem C*. 2019;123(14):9001.
8. Herzing AA, Kiely CJ, Carley AF, Landon P, Hutchings GJ. Identification of active gold nanoclusters on iron oxide supports for CO oxidation. *Science*. 2008;321(5894):1331.
9. Yoo E, Okata T, Akita T, Kohyama M, Nakamura J, Honma I. Enhanced electrocatalytic activity of Pt subnanoclusters on graphene nanosheet surface. *Nano Lett*. 2009;9(6):2255.
10. Guo LW, Du PP, Fu XP, Ma C, Zeng J, Si R, et al. Contributions of distinct gold species to catalytic reactivity for carbon monoxide oxidation. *Nat Commun*. 2016;7:13481.
11. Wang X, Du LY, Du M, Ma C, Zeng J, Jia CJ, et al. Catalytically active ceria-supported cobalt-manganese oxide nanocatalysts for oxidation of carbon monoxide. *Phys Chem Chem Phys*. 2017;19(22):14533.
12. Hendriksen BL, Frenken JW. CO oxidation on Pt(110): scanning tunneling microscopy inside a high-pressure flow reactor. *Phys Rev Lett*. 2002;89(4):046101.
13. Chen MS, Cai Y, Yan Z, Gath KK, Axnanda S, Goodman DW. Highly active surfaces for CO oxidation on Rh, Pd, and Pt. *Surf Sci*. 2007;601(23):5326.
14. Bonanni S, Ait-Mansour K, Harbich W, Brune H. Effect of the TiO_2 reduction state on the catalytic CO oxidation on deposited size-selected Pt clusters. *J Am Chem Soc*. 2012;134(7):3445.
15. Liu LQ, Zhou F, Wang LG, Qi XJ, Shi F, Deng YQ. Low-temperature CO oxidation over supported Pt, Pd catalysts: particular role of FeO_x support for oxygen supply during reactions. *J Catal*. 2010;274(1):1.
16. Bi W, Hu YJ, Jiang H, Yu H, Li WG, Li CZ. *In-situ* synthesized surface N-doped Pt/TiO_2 via flame spray pyrolysis with enhanced thermal stability for CO catalytic oxidation. *Appl Surf Sci*. 2019;481:360.
17. Qiao BT, Wang AQ, Yang XF, Allard LF, Jiang Z, Cui YT, et al. Single-atom catalysis of CO oxidation using Pt_1/FeO_x. *Nat Chem*. 2011;3(8):634.
18. Li J, Tang Y, Ma YY, Zhang ZY, Tao F, Qu YQ. *In situ* formation of isolated bimetallic PtCe sites of single-dispersed Pt on CeO_2 for low-temperature CO oxidation. *ACS Appl Mater Interfaces*. 2018;10(44):38134.
19. Bera P, Gayen A, Hegde MS, Lalla NP, Spadaro L, Frusteri F, et al. Promoting effect of CeO_2 in combustion synthesized Pt/CeO_2 catalyst for CO oxidation. *J Phys Chem B*. 2003;107(25):6122.
20. Moses-DeBusk M, Yoon M, Allard LF, Mullins DR, Wu Z, Yang X, et al. CO oxidation on supported single Pt atoms: experimental and *ab initio* density functional studies of CO interaction with Pt atom on theta-Al_2O_3(010) surface. *J Am Chem Soc*. 2013;135(34):12634.
21. Fu Q, Saltsburg H, Flytzani-Stephanopoulos M. Active nonmetallic Au and Pt species on ceria-based water-gas shift catalysts. *Science*. 2003;301(5635):935.
22. Wang X, Li Y. Rare-Earth-compound nanowires, nanotubes, and fullerene-like nanoparticles: synthesis, characterization, and properties. *Chem-Eur J*. 2003;9(22):5627.
23. Wang K, Yao QL, Qing SJ, Lu ZH. La(OH)$_3$ nanosheet-supported CoPt nanoparticles: a highly efficient and magnetically recyclable catalyst for hydrogen production from hydrazine in aqueous solution. *J Mater Chem A*. 2019;7(16):9903.
24. Tian Y, Zhao Y, Zhang YG, Ricardez-Sandoval L, Wang X, Li JD. Construction of oxygen-deficient La(OH)$_3$ nanorods wrapped by reduced graphene oxide for polysulfide trapping toward high-performance lithium/sulfur batteries. *ACS Appl Mater Interfaces*. 2019;11(26):23271.
25. Okada R, Kawanishi K, Katagiri K, Inumaru K. Ammonolysis-free synthesis of $La_2O_2CN_2$ by cyanamidation of La(OH)$_3$ using urea, and its photoluminescence properties. *Ceram Int*. 2019;45(7):9325.
26. Aghazadeh M, Arhami B, Malek Barmi A-A, Hosseinifard M, Gharailou D, Fathollahi F. La(OH)$_3$ and La_2O_3 nanospindles prepared by template-free direct electrodeposition followed by heat-treatment. *Mater Lett*. 2014;115:68.
27. Li XY, Niu LJ, Zhang XL, Duan D, Li K, Sun Z. Fabrication of Ag/La(OH)$_3$ nanorod framework composites through dealloying for CO oxidation. *JOM*. 2018;71(2):522.

28. Kang J-G, Kim Y-I, Won C-D, Sohn Y. Synthesis and physicochemical properties of $La(OH)_3$ and La_2O_3 nanostructures. *Mater Sci Semicond Process*. 2015;40:737.
29. Wang LG, Ma YB, Wang Y, Liu SM, Deng YQ. Efficient synthesis of glycerol carbonate from glycerol and urea with lanthanum oxide as a solid base catalyst. *Catal Commun*. 2011;12(15):1458.
30. Zhang Z, Verykios XE. Carbon dioxide reforming of methane to synthesis gas over Ni/La_2O_3 catalysts. *Appl Catal A-Gen*. 1996;138(1):109.
31. Chen YZ, Li HL, Zhao WH, Zhang WB, Li JW, Li W, et al. Optimizing reaction paths for methanol synthesis from CO_2 hydrogenation via metal-ligand cooperativity. *Nat Commun*. 2019;10(1):1885.
32. Peng YH, Geng ZG, Zhao ST, Wang LB, Li HL, Wang X, et al. Pt single atoms embedded in the surface of Ni nanocrystals as highly active catalysts for selective hydrogenation of nitro compounds. *Nano Lett*. 2018;18(6):3785.
33. Yin XP, Wang HJ, Tang SF, Lu XL, Shu M, Si R, et al. Engineering the coordination environment of single-atom platinum anchored on graphdiyne for optimizing electrocatalytic hydrogen evolution. *Angew Chem Int Ed*. 2018;57(30):9382.
34. Hou FJ, Zhao HH, Song HL, Chou LJ, Zhao J, Yang J, et al. Effect of impregnation strategy on catalytic hydrogenation behavior of PtCo catalysts supported on $La_2O_2CO_3$ nanorods. *J Rare Earths*. 2018;36(9):965.
35. Huang XY, Dang CX, Yu H, Wang HJ, Peng F. Morphology effect of $Ir/La_2O_2CO_3$ nanorods with selectively exposed {110} facets in catalytic steam reforming of glycerol. *ACS Catal*. 2015;5(2):1155.
36. Zhai Y, Pierre D, Si R, Deng W, Ferrin P, Nilekar AU, et al. Alkali-stabilized $Pt-(OH)_x$ species catalyze low-temperature water-gas shift reactions. *Science*. 2010;329(5999):1633.
37. Zhou AB, Wang J, Wang H, Li H, Wang JQ, Shen MQ. Effect of active oxygen on the performance of Pt/CeO_2 catalysts for CO oxidation. *J Rare Earths*. 2018;36(3):257.
38. Nan B, Hu XC, Wang X, Jia CJ, Ma C, Li MX, et al. Effects of multiple platinum species on catalytic reactivity distinguished by electron microscopy and X-ray absorption spectroscopy techniques. *J Phys Chem B*. 2017;121(46):25805.
39. Wang HL, Liu MH, Ma Y, Gong K, Liu W, Ran R, et al. Simple strategy generating hydrothermally stable core–shell platinum catalysts with tunable distribution of acid sites. *ACS Catal*. 2018;8(4):2796.
40. Sun J, Kyotani T, Tomita A. Preparation and characterization of lanthanum carbonate hydroxide. *J Solid State Chem*. 1986;65(1):94.
41. Yang M, Li S, Wang Y, Herron JA, Xu Y, Allard LF, et al. Catalytically active $Au-O(OH)_x$-species stabilized by alkali ions on zeolites and mesoporous oxides. *Science*. 2014;346(6216):1498.